Initial Evaluation of ^{18}F-GE-179, a Putative PET Tracer for Activated *N*-Methyl D-Aspartate Receptors

Colm J. McGinnity[1,2], Alexander Hammers[1–5], Daniela A. Riaño Barros[1,2], Sajinder K. Luthra[6], Paul A. Jones[6], William Trigg[6], Caroline Micallef[4,5], Mark R. Symms[4,5], David J. Brooks[1,6], Matthias J. Koepp[2,4,5], and John S. Duncan[2,4,5]

[1]Division of Brain Sciences, Department of Medicine, Imperial College London, London, United Kingdom; [2]MRC Clinical Sciences Centre, London, United Kingdom; [3]The Neurodis Foundation, CERMEP—Imagerie du Vivant, Lyon, France; [4]Department of Clinical and Experimental Epilepsy, UCL Institute of Neurology, London, United Kingdom; [5]Epilepsy Society, Chalfont St. Peter, United Kingdom; and [6]GE Healthcare plc, Amersham, United Kingdom

N-methyl D-aspartate (NMDA) ion channels play a key role in a wide range of physiologic (e.g., memory and learning tasks) and pathologic processes (e.g., excitotoxicity). To date, suitable PET markers of NMDA ion channel activity have not been available. ^{18}F-GE-179 is a novel radioligand that selectively binds to the open/active state of the NMDA receptor ion channel, displacing the binding of ^{3}H-tenocyclidine from the intrachannel binding site with an affinity of 2.4 nM. No significant binding was observed with 10 nM GE-179 at 60 other neuroreceptors, channels, or transporters. We describe the kinetic behavior of the radioligand in vivo in humans. **Methods:** Nine healthy participants (6 men, 3 women; median age, 37 y) each underwent a 90-min PET scan after an intravenous injection of ^{18}F-GE-179. Continuous arterial blood sampling over the first 15 min was followed by discrete blood sampling over the duration of the scan. Brain radioactivity (KBq/mL) was measured in summation images created from the attenuation- and motion-corrected dynamic images. Metabolite-corrected parent plasma input functions were generated. We assessed the abilities of 1-, 2-, and 3-compartment models to kinetically describe cerebral time–activity curves using 6 bilateral regions of interest. Parametric volume-of-distribution (V_T) images were generated by voxelwise rank-shaping regularization of exponential spectral analysis (RS-ESA). **Results:** A 2-brain-compartment, 4-rate-constant model best described the radioligand's kinetics in normal gray matter of subjects at rest. At 30 min after injection, 37% of plasma radioactivity represented unmetabolized ^{18}F-GE-179. The highest mean levels of gray matter radioactivity were seen in the putamina and peaked at 7.5 min. A significant positive correlation was observed between K_1 and V_T (Spearman $\rho = 0.398$; $P = 0.003$). Between-subject coefficients of variation of V_T ranged between 12% and 16%. Voxelwise RS-ESA yielded similar V_Ts and coefficients of variation. **Conclusion:** ^{18}F-GE-179 exhibits high and rapid brain extraction, with a relatively homogeneous distribution in gray matter and acceptable between-subject variability. Despite its rapid peripheral metabolism, quantification of ^{18}F-GE-179 V_T is feasible both within regions of interest and at the voxel level. The specificity of ^{18}F-GE-179 binding, however, requires further characterization with in vivo studies using activation and disease models.

N-methyl-D-aspartate (NMDA) receptors for L-glutamate, the major excitatory neurotransmitter in the central nervous system (CNS), are linked to ligand- and voltage-gated ion channels (*1*). Excitatory synaptic transmission via these receptors mediates neuroplasticity and is necessary for learning and memory. In pathologic circumstances, however, NMDA receptor overactivation may be associated with cell death (*2*).

Excessive NMDA receptor activation mediates excitotoxic neuronal injury after acute cerebral insults (*3*) and is thought to contribute to disorders of neuronal hyperexcitability (e.g., epilepsy) and chronic neurodegenerative (e.g., Alzheimer, Huntington) (*4*) and psychotic (*5*) disorders. Hence, there is interest in the development of radioligands to allow assessment of NMDA receptor function in humans in vivo.

Imaging NMDA ion channel function in vivo in humans has been challenging because of low brain uptake, low affinity for the NMDA receptor, high rates of dissociation, rapid metabolism, and high nonspecific binding of candidate tracers. To date, only 6 of more than 60 radioligands designed for in vivo imaging of the NMDA receptor system (*6*) have progressed to PET or SPECT studies in humans (Table 1). Of these, 5 act at the phencyclidine recognition site (*7*), which lies within the NMDA ion channel pore, and hence these radioligands require receptor activation to allow binding. The diarylguanidine CNS 5161, a noncompetitive antagonist, is one such use-dependent ligand that demonstrated high uptake in the putamen and thalamus in human studies in vivo (*8–10*). Quantification of ^{11}C-CNS 5161 proved to be difficult, its radiochemical yield low, and its metabolism fast; thus, it was not pursued as a PET radioligand.

In vitro evaluation of a ^{18}F-labeled analog of CNS 5161 (^{18}F-GE-179 (*11*)) showed that ^{18}F-GE-179 displaces ^{3}H-TCP (-^{3}H-N-(1-[thienyl] cyclohexyl)piperidine) from the phencyclidine site with a Ki (inhibition constant) of 2.4 nM (similar to that seen with ^{3}H-MK-801 (^{3}H-(+)-5-methyl-10,11-dihydro-5H-dibenzo[a,d]cyclohepten-5,10-imine maleate) and CNS 5161 (*12*)) and GE-179 inhibits glutamate-mediated influx of Ca^{2+} in teratocarcinoma 2 (NT2) cells differentiated to express human NMDA receptors in a dose-dependent manner (supplemental data; supplemental mate-

TABLE 1
Healthy Participant Population Demographics, MR Imaging Findings, and ^{18}F-GE-179 Injection Data

Patient identification no.	Age (y)	Sex	Weight (kg)	Handedness	Smoker	MR imaging	Injected dose (MBq)	Specific activity at time of injection (GBq/μmol)	Purity (%)	Coinjected mass (μg)
1	26	M	80	L	No	Normal	187.0	450.1	98	0.16
2	31	M	67	R	No	Normal	173.2	73.1	97	0.91
3	55	M	83	R	Yes	WM foci	186.0	1428.0	97	0.05
4	37	F	58	R	No	Tiny WM foci	180.4	769.5	96	0.09
5	61	M	65	R	No	Normal	183.7	881.5	95	0.08
6	62	F	53	R	No	WM foci	185.3	229.5	96	0.31
7*	25	F	81	R	No	Normal	192.4	263.8	96	0.28
8	26	M	91	L	No	Normal	189.2	726.6	96	0.10
9	57	M	84	R	No	RF WM foci	186.9	311.9	96	0.23
Median/total	37	6 M	80	7 right	1 smoker	NA	186.0	450.1	96	0.16
CV (%)			17				2.8	70.0	1	102
IQR	26–57		65–83				183.7–187.0	263.8–769.5	96–97	0.09–0.28
Minimum	25		53				173.2	73.1	95	0.05
Maximum	62		91				192.4	1428.0	98	0.91

*Participant 7 was a regular user of ibuprofen. Analysis by ANOVA failed to demonstrate any significant influence of this variable on AUC_{metabs} or AUC_{IF}.

WM = white matter; RF = right frontal; NA = nonapplicable.

rials are available at http://jnm.snmjournals.org). GE-179 has a distribution coefficient (log $D_{7.4}$) of 2.49 ± 0.1 (11), similar to that of CNS 5161 (log $P = 1.92 \pm 0.26$ (13)) and indicative of moderate lipophilicity. In a binding study to characterize GE-179 binding to CNS targets other than the NMDA phencyclidine site, 10 nM GE-179 did not significantly bind to any of the 60 receptors, channels, and transporters assessed. Binding of ^{3}H-ifenprodil to the rat σ 2 receptor was only inhibited by 8%; all other targets were either inhibited by 3% or less at 10 nM or had not shown significant binding ($\pm20\%$ inhibition) at the higher dose of 1 μM (supplemental data).

Here, to our knowledge, we report the first-in-human use of ^{18}F-GE-179 PET in healthy human subjects. Our primary objective was to evaluate the kinetic behavior of the radioligand in vivo in normal human brain.

MATERIALS AND METHODS

This study was approved by the Research Ethics Committees of the Royal Marsden Hospital, Imperial College Healthcare NHS Trust, and University College London Hospitals NHS Foundation Trust. Permission to administer ^{18}F-GE-179 was obtained from the Administration of Radioactive Substances Advisory Committee, U.K. All participants provided written, informed consent before participation.

Nine healthy participants without history of neurologic or psychiatric illness were scanned. The demographic and descriptive data for the subjects are presented in Table 1.

^{18}F-GE-179 was synthesized by Hammersmith Imanet Limited as previously described (11). Details of the injectate are presented in Table 1.

PET Image Acquisition and Preprocessing

Images were acquired using an ECAT EXACT3D 962 HR+ PET camera (Siemens/CTI) with a 15.5-cm axial and 58.0-cm transaxial field of view. After a transmission scan, each subject underwent a 90-min dynamic emission scan following an intravenous bolus injection of median 186 MBq of ^{18}F-GE-179. Thirty-four frames of increasing duration were acquired. Data were reconstructed using a Fourier rebinning algorithm

(FORE; (14)) and 2-dimensioanl filtered backprojection (ramp, kernel 2.0 mm in full width at half maximum). The voxel size of the reconstructed images was $2.092 \times 2.092 \times 2.42$ mm.

The images were acquired in a quiet, dimly lit room without background noise. Head position was monitored throughout with the camera's laser light. Continuous arterial blood sampling at a rate of 5 mL per minute was performed from 0 to 15 min. Discrete arterial blood samples were taken at baseline and a further 8 times during the next 90.5 min. High-performance liquid chromatography was used to quantify radiolabeled metabolites in the plasma.

The fraction of plasma radioactivity attributable to the parent ^{18}F-GE-179 was fitted to a sigmoid function normalized to unity at 0 min using CLICKFIT version1.7 (Hinz R, Cunningham VJ, Imaging Research Solutions Limited, London, U.K.) running in MATLAB 6.5 (The MathWorks Inc.) to generate a metabolite model for each participant.

The area under the metabolite model curve (AUC_{metabs}) was used as a measure of the rate of metabolism for each individual. Correlations between the AUC_{metabs} and age, weight, and body mass index (BMI) were examined by Spearman rank (ρ) correlation coefficient using SPSS (version 16.0 [SPSS Inc., IBM Corp.] for Windows [Microsoft]). The threshold of statistical significance ($P < 0.05$) was corrected for multiple comparisons using the Bonferroni method.

Continuous decay- and metabolite-corrected parent plasma input functions were generated for all subjects using CLICKFIT, as described previously (15). Briefly, the final input functions were generated by multiplication of the calibrated time course of radioactivity in the blood with the fits to the plasma-to-blood ratios and metabolite fractions. Rodent in vivo metabolism data showed that the likelihood of ingress of radiolabeled metabolites in to the CNS was low; this, therefore, was not accounted for (see supplemental data). The areas under the decay- and metabolite-corrected parent plasma input function curves (AUC_{IF}) were calculated for each subject by summation of the counts in the parent plasma input function file, after correction for ^{18}F radiodecay.

Correlations between the AUC_{IF} and age, weight, BMI, and injected dose were examined by Spearman rank (ρ) correlation coefficient.
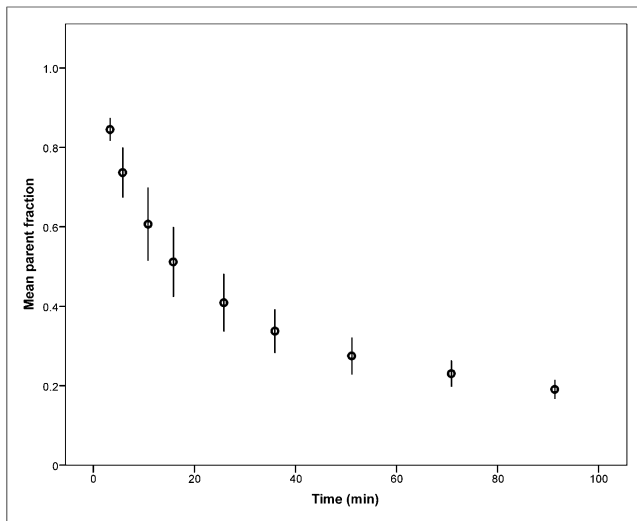
FIGURE 1. Mean fraction of parent ^{18}F-GE-179 remaining in plasma. Error bars represent the 95% confidence interval for the mean at each time point.

We hypothesized a priori that the AUC_{IF} would be negatively correlated with weight or BMI and positively correlated with injected dose; these correlations were not, therefore, corrected for multiple comparisons.

Attenuation-corrected dynamic PET images were corrected for head motion using a post hoc frame-to-frame realignment method running in MATLAB 7.4, with the corresponding nonattenuated image used as a reference (Piwave8.0, internal software (16)). Summation images (KBq/mL) that were weighted relative to frame duration were created for 5–30, 30–60, and 60–90 min from the attenuation- and motion-corrected dynamic image file using Receptor Parametric Mapping (version 6 (17)) software running in MATLAB 5.0.

Global and Regional Distribution of Radioactivity

Global (whole-brain) radioactivity concentration (i.e., uptake [KBq/mL]) in the summation images was computed using a whole-brain mask, which was created for each of the 9 participants from their 5- to 30-min summed images using the extract region tool implemented in Analyze8.1 (AnalyzeDirect, Inc.); the mean over the entire matrix within this mask was then computed.

Radioactivity concentration in the gray matter of the summation images was computed as follows. First, an individualized gray matter mask was created for each of the 9 participants by segmentation of their T1-weighted MR image according to the Unified Segmentation method (18) implemented in SPM8 (Statistical Parametric Mapping 8; Wellcome Trust Centre for Neuroimaging, UCL, London) and by thresholding of the resulting gray matter probability map at 0.5 using Analyze 8.1. The 9 individual participants' MR images and gray matter masks were coregistered to their 5- to 30-min summation images, before calculation of the mean radioactivity concentration. White matter radioactivity concentrations were computed with white matter masks that were created simultaneously.

An 83-region gray matter–only region-of-interest (ROI) map was produced for each of the 9 participants by transformation of 30 manually created atlases (19) to the participant's native MR imaging space using multiatlas propagation with enhanced registration and decision fusion (20). The resulting atlas was then multiplied by the thresholded gray matter component of the MR image and used to sample the radioactivity concentration (KBq/mL) in each of the 83 regions.

The median radioactivity concentrations were calculated for the participants, surveying all 83 regions and combining left and right homologs where possible.

The median asymmetry indices (AIs) were calculated to compare radioactivity concentration (R_C) in the ROIs highlighted by the survey, according to the following formula:

$$AI = \frac{R_{C\_Left} - R_{C\_Right}}{\left(R_{C\_Left} + R_{C\_Right}\right)/2}$$

Compartmental Modeling of ^{18}F-GE-179 Cerebral Tissue Kinetics

Six gray matter–only ROIs were defined a priori for modeling purposes according to the known distribution of the NMDA receptor (21) and sampled with left and right sides combined. In order of decreasing approximate receptor density, the ROIs were the putamina, thalami, superior frontal gyri, parahippocampal gyri, occipital lobes, and cerebellum. The entire brain gray matter and white matter ROIs were also sampled. Each participant's attenuation- and motion-corrected dynamic PET image was sampled over all 34 time frames. Time–activity curves for each ROI were produced using CLICKFIT from the scanner information file and a weights file that had been generated for each ROI from the sampled dynamic PET data.

Analyses of ^{18}F-GE-179 cerebral tissue kinetics were performed using the following standard compartmental models: 1-brain-compartment, 2-rate constant (1c2kbv, reversible binding); 2-brain-compartment, 3-rate-constant (2c3kbv, irreversible binding); 2-brain-compartment, 4-rate-constant (2c4kbv, reversible binding); and 3-brain-compartment, 6-rate-constant (3c6kbv, reversible binding). All models incorporated a variable blood volume component and were used to calculate the delay between plasma and tissue time–activity curves.

The model fit was assessed using the Akaike Information Criterion (AICw) and the intraregion and between-subject coefficient of variation (CV) of volume-of-distribution (V_T) estimates.

Strengths of regional V_T and K_1 correlations were assessed by Spearman rank (ρ) correlation coefficients, pooling all ROI data for the 9 participants.

The correlations between gray matter V_T and age, weight, BMI, injected dose, specific radioactivity at the time of injection, and AUC_{IF} were similarly interrogated with the Spearman rank (ρ) statistic, with correction for multiple comparisons using Bonferroni method.

Generation of Parametric V_T Images

Parametric V_T images were generated by voxelwise rank-shaping regularization of exponential spectral analysis (RS-ESA) (22). RS-ESA is a development of the model-free exponential spectral analysis
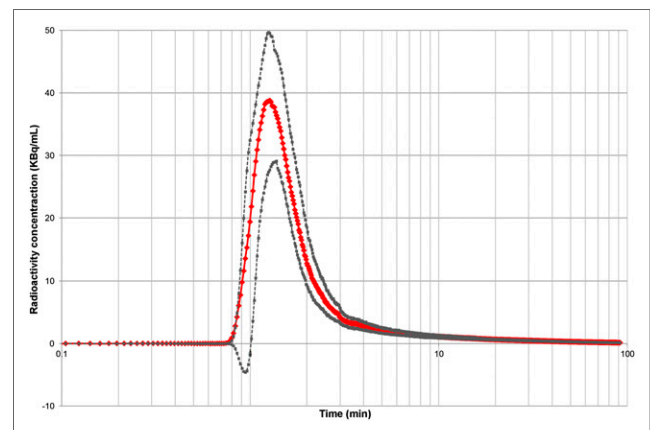
FIGURE 2. Mean decay- and metabolite-corrected parent plasma input function. Red line models mean radioactivity concentration attributed to parent ^{18}F-GE-179 in plasma at each time point. Gray squares represent 95% confidence intervals for mean at each time point.

TABLE 2
Regional Radioactivity Concentration and Asymmetry Index

Region	Radioactivity concentration (KBq/mL)		Between-subject CV (%)	Asymmetry index	
	Median	IQR		Median	IQR
Putamina	8.7	6.8–11.6	27.7	0.00	–0.02–0.02
Cunei	8.4	7.0–11.3	29.2	0.00	–0.02–0.02
Lingual gyri	8.3	6.9–10.9	27.4	0.03	0.00–0.05
Thalami	8.3	6.6–11.2	26.9	−0.03	–0.05–0.01
Cerebellum	7.6	6.2–9.7	26.7	0.00	–0.02–0.01
Superior frontal gyri	7.5	6.0–9.4	26.1	0.01	–0.02–0.01
Hippocampi	6.7	5.5–8.6	28.2	−0.01	–0.04–0.02
Parahippocampal gyri	6.1	4.9–7.6	26.5	−0.03	–0.06–0.00
Anterior medial temporal lobes	6.0	4.8–7.5	25.4	−0.00	0.00–0.06
White matter	6.0	4.5–7.8	28.1	NA	NA

Radioactivity concentration is uptake of ^{18}F-GE-179 at 5–30 min.
NA = not applicable.

estimation method (23) that has been optimized for noisy datasets by incorporating a singular value decomposition of the exponential base. Time constants were specified as 5 and 5,100 s. The noise fraction was specified as 0.15.

The median V_T was computed within the ROIs and compared with the V_Ts derived via compartmental modeling. The correlations between regional V_Ts derived using each method were assessed by Spearman rank (ρ) correlation coefficient, pooling all ROI data for the 9 participants.

RESULTS

Metabolism

Unmetabolized ^{18}F-GE-179 accounted for a mean of 50% of the plasma radioactivity at approximately 16 min and 25% at 44 min (Fig. 1).

There was a significant negative correlation between the AUC$_{metabs}$ and BMI ($r = −0.86$, $P = 0.002$). There were no significant correlations with other variables.

FIGURE 3. Time–activity curves: percentage of injected dose of ^{18}F-GE-179 per mL versus time. Data have been decay-corrected.

Decay- and Metabolite-Corrected Parent Plasma Input Functions

The parent plasma input functions peaked at a median of 71.5 s (interquartile range [IQR], 65.6–81.7 s) and decreased to less than 10% of the peak activity concentration within 5 min (Fig. 2). The radioactivity concentrations in plasma at the peak of the parent plasma input functions had a median of 47.3 kBq/mL (IQR, 43.4–65.1 kBq/mL), equivalent to 0.02% of the injected dose/mL.

The median AUC$_{IF}$ was 4782.0 kBq·cm^{-3} (IQR, 4,165.4–5,754.8 kBq/mL). There was a significant negative correlation between the AUC$_{IF}$ and weight and AUC$_{IF}$ and BMI (both $r = −0.721$, $P = 0.019$). There were no significant correlations with other variables.
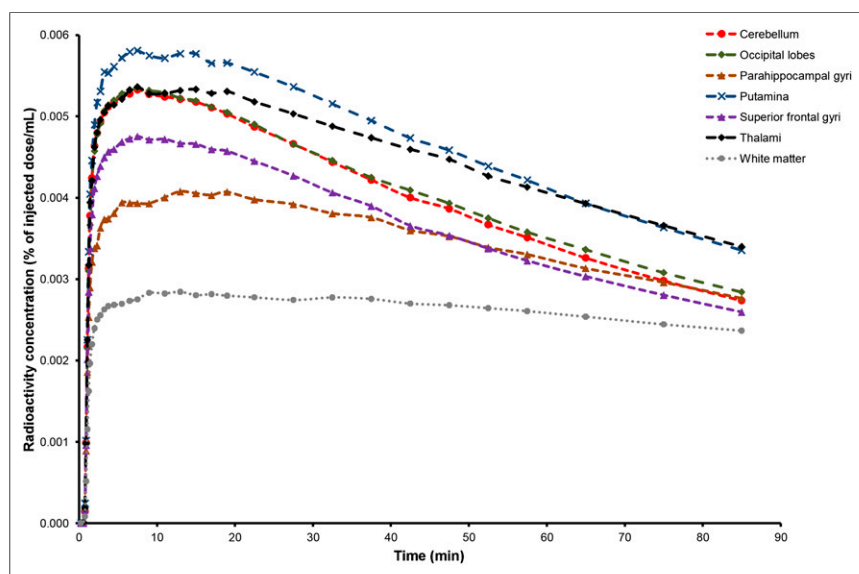
Regional Distribution of Radioactivity

The median gray matter radioactivity concentration was 7.3 kBq/mL (IQR, 5.9–9.2 kBq/mL) in the 5- to 30-min summation images. The highest median radioactivity concentration was identified in the putamina, followed by (in descending order) the cunei, lingual gyri, thalami, and cerebellum (Table 2). The between-subject CVs for the gray matter radioactivity concentration ranged from 25.4% to 29.2%.

The lowest median radioactivity concentration in gray matter was observed in the anterior medial temporal lobes, followed by (in ascending order) the parahippocampal gyri, hippocampi, and superior frontal gyri (Table 2).

Left–Right Asymmetry of ^{18}F-GE-179 Radioactivity Concentration

The range of median asymmetry indices in the regions reported above was from –0.03 (IQR, –0.05–0.01) in the thalami to 0.03 (IQR, 0.00–0.05) in the lingual gyri (Table 2).

TABLE 3
^{18}F-GE-179 V_T and K_1 as Calculated by Regional 2-Brain-Compartment, 4-Rate-Constant Model

Region	AICw		K_1 (× 10^{-3})	V_T		Between-subject CV in V_T (%)
	Median	IQR		Median	IQR	
(Whole-brain) gray matter*	−207.7	−203.1 to −219.8	3.6	8.9	8.5–9.4	12.9
Putamina	−149.1	−115.3 to −159.3	4.6	11.7	9.9–12.7	15.9
Thalami	−146.6	−145.1 to −147.4	4.5	11.8	10.4–13.0	15.8
Superior frontal gyri	−182.4	−142.9 to −186.7	3.9	8.6	8.4–9.2	12.9
Occipital lobes	−207.1	−198.6 to −212.4	4.1	9.5	8.8–10.7	13.7
Cerebellum	−191.6	−186.6 to −209.6	4.0	8.9	8.0–10.2	13.5
Parahippocampal gyri	−160.9	−149.7 to −179.2	3.1	9.3	8.1–9.7	16.0

*Data are derived from 8 participants as model failure noted in (whole-brain) gray matter for participant 4.

Time–Activity Curves

The mean gray matter radioactivity concentration peaked at 8.9 kBq/mL, equivalent to a mean of 0.0048 percentage injected dose (%ID) at 7.5 min. The mean white matter radioactivity peaked at 5.1 kBq/mL (0.0028 %ID) at 13 min. The radioactivity declined more quickly in gray than in the white matter.

The highest mean gray matter radioactivity concentration was seen in the putamina, which peaked at 10.4 kBq/mL (0.0056 %ID) at 7.5 min (Fig. 3), followed by the thalami, occipital lobes, cerebellum, superior frontal gyri, and parahippocampal gyri. The radioactivity concentration in the putamina decreased to approximately 58% of the peak at 91.5 min, to 63% in the thalami, 53% in the occipital lobes, 51% in the cerebellum, and 64% in the superior frontal gyri. The radioactivity concentration peaked at 13 min in the parahippocampal gyri, later than in other ROIs, but also declined more slowly than in the other gray matter regions (68% of the peak at 91.5 min).

Compartmental Modeling of ^{18}F-GE-179 Cerebral Tissue Kinetics

The 2c4kbv model best described the radioligand's kinetics in gray matter (AICw = −207; Table 3; Fig. 4), with a slight bias
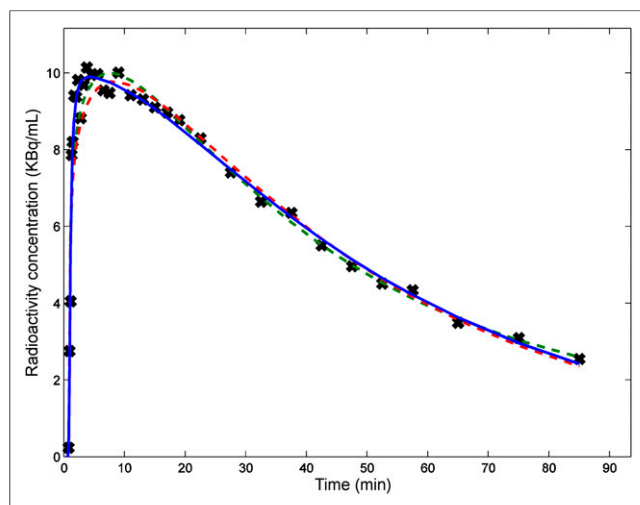
FIGURE 4. Compartmental modeling of ^{18}F-GE-179 left putamen tissue kinetics. Black crosses indicate radioactivity concentration measured from left putamen at each time point. Red line represents 1c2kbv model fit, green line represents 2c3kbv model fit, and blue line represents 2c4kbv model fit.

overestimation of peak radioactivity concentration. In contrast, the 1c2kbv and 2c3kbv models were characterized by consistently higher AICw, for example, −114, in gray matter, and the 3c6kbv model was characterized by a large number of outlier values within each ROI.

The median estimates of V_T in each ROI, derived by application of the 2c4kbv models to individual time–activity curves, are shown in Table 3. The between-subject CVs for V_T in gray matter regions ranged from 12.9% to 16.0%.

A positive correlation was detected between V_T and K_1 (Spearman ρ = 0.398; P = 0.003; Fig. 5).

There was a positive correlation between gray matter V_T and age (Spearman ρ = 0.803; P = 0.009). There were no significant correlations with other variables.

Voxelwise Rank-Shaping (RS-ESA)

A representative example of an ^{18}F-GE-179 V_T image is provided in Figure 6. RS-ESA yielded V_Ts (Table 4) that correlated with those derived from regional compartmental modeling (Spearman ρ = 0.901; P < 0.001; Fig. 5). The between-subject CVs for V_T in gray matter regions ranged from 11.6% to 14.8%. A bias toward underestimation of V_T, relative to that derived from the 2c4kbv model, was observed (Fig. 7).

DISCUSSION

To our knowledge, we describe the first use of ^{18}F-GE-179 as a PET radioligand in humans.

Brain penetration of ^{18}F-GE-179 was high, with a mean peak radioactivity concentration of 8.9 kBq/mL in gray matter, which is greater than that achieved when using the NMDA radioligands ^{18}F-memantine (24), ^{11}C-AcL703 (25), and ^{11}C-CNS 5161 (8), normalized to injected volume. The mean peak global and gray matter radioactivity concentrations have not been reported with other radioligands targeted at the NMDA receptor (26–30).

The distribution of radioactivity in gray matter after injection of ^{18}F-GE-179 was relatively homogeneous, with the highest concentration (in the absence of correction for partial-volume effects) observed in the putamina, a region of moderate NMDA receptor density (31). Peak and summed (5–30 min) radioactivity concentrations in the white matter, often considered a reference region for nonspecific binding (32), were just over half that of the putamina. High radioactivity concentration was observed in the cerebellar cortex, in keeping with the documented existence of NMDA receptors in this region (33).

The channel maximal open probability of the NR2A subunit is approximately 2–5 times higher than that of the NR2B subunit
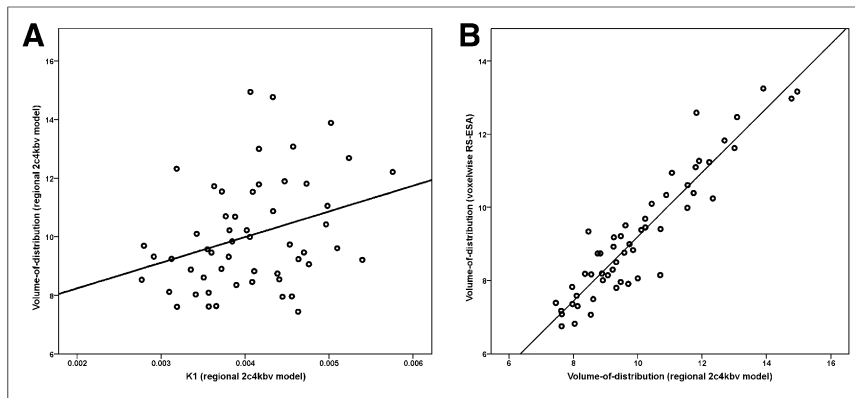
FIGURE 5. (A) ^{18}F-GE-179 V_T versus K_1, both as calculated by regional 2c4kbv model. (B) ^{18}F-GE-179 V_T as calculated by voxelwise RS-ESA versus ^{18}F-GE-179 V_T as calculated by regional 2c4kbv model. Data from 6 bilateral ROIs are shown for each participant.

(*34*), 50 times higher than that of the NR2C (*35*), and 9 times higher than that of NR2D subunits (*36*). NMDA receptors are particularly concentrated in the hippocampi (*31*), with NR2B subunits present in higher concentrations than NR2A (*37*); the lower channel opening probabilities of this subunit might underlie the modest radioactivity concentration observed in medial temporal regions, which was nearly equivalent to that seen in white matter. We also observed low radioactivity concentration in the brain stem, which is consistent with the lack of NR2A and NR2B expression in this region (*37*), suggesting specificity of gray matter binding. However, our finding of a weak-to-moderate positive correlation between K_1 and V_T suggests partial cerebral blood flow-dependency.

Ideally, the specificity of ^{18}F-GE-179 binding in vivo would be quantified by coadministration of unlabeled GE-179 or another unlabeled agent with high affinity and selectivity for the phencyclidine-binding site. However, this is not feasible in humans because of poor tolerability of blocking doses of NMDA antagonists. A dose-escalation safety study with CNS 5161 was abandoned after a sustained systolic blood pressure increase in 1 of 2 participants administered 750 μg (*38*). The performance of a cognitive task, such as an episodic memory task, during radioligand injection might be expected to increase specific binding in certain brain areas, that is, in the medial temporal lobe. However, such a paradigm would have to be performed for approximately 20 min or more because of the rate of uptake of the radioligand, a second baseline scan at rest would be required, and the increased local
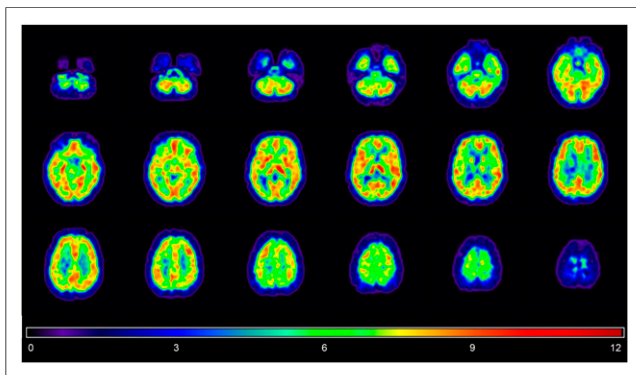
cerebral blood flow would confound the analyses. Focal epileptic activity could also be hypothesized to increase (specific) binding in the medial temporal lobe regions. ^{18}F-GE-179 will be investigated in participants with epilepsy in a subsequent study.

Additional limitations of this first-in-human study include the small sample size and lack of test–retest data. A further study is required to demonstrate acceptable within-subject (i.e., test– retest) variability for the quantification of ^{18}F-GE-179 V_T. However, in view of the low NMDA–channel opening probability at baseline, test–retest data at rest without control over cognitive and emotional state might not be helpful.

The rate of metabolism of ^{18}F-GE-179 was less rapid than that of ^{11}C-CNS 5161 (*8*) and ^{123}I-CNS 1261 (*29*) but not ^{18}F-memantine (*24*) (data not reported for other NMDA-receptor radioligands). Our analyses assumed radiolabeled metabolites did not penetrate the brain, although 1 more polar compound was identified in rodent brains at 30 min after injection (GE Healthcare, unpublished data, on file, 2009). Parent ^{18}F-GE-179 accounted for 84% of the cerebral radioactivity at this point. In humans, the slower plasma metabolism of the radioligand suggests it should account for an even greater proportion at this time point.

^{18}F-GE-179 exhibited faster gray matter tissue uptake and washout than ^{11}C-CNS 5161 (*8*) (and also ^{123}I-MK-801 (*28,30*), ^{18}F-memantine (*24*), and ^{11}C-AcL703 (*25*)). Model fits indicated a better fit for the reversible model. Our data indicate that quantification of regional ^{18}F-GE-179 V_T is achievable with a 2c4kbv with variable blood component. Voxelwise quantification of ^{18}F-GE-179 V_T by RS-ESA yielded comparable estimates and parametric maps of acceptable visual quality; this will also allow for comparison of V_T between populations without a priori delineation of ROI whereas voxelwise compartmental modeling is hampered by noise. When ROI quantification is preferred, we suggest that the 2c4kbv model is used to avoid the negative bias associated with RS-ESA. However, the choice of quantification method will also be informed by test–retest variability, when such data become available.

^{18}F-GE-179 uptake and V_T have acceptable between-subject variability in healthy participants, as evidenced by regional between-subject CVs of less than 16%. A positive correlation between V_T and age was observed and so future studies, especially if involving poorly matched subgroups, should model this as a covariate in the analyses. This finding appears at odds with the age-related declines in cerebral blood flow (*39*) and NMDA receptor function (*40*). However, it is possible that the relationship between ^{18}F-GE-179 V_T and age is nonlinear. In such a case, the positive correlation we have identified might reflect the limited age spread (range, 25–62 y) of our cohort. As expected, participants of higher weight or BMI had a lower parent plasma input than the remaining controls. Moreover, regional V_T was seen to correlate with the first rate constant (i.e., linked to cerebral blood flood).

CONCLUSION

Our first-in-human evaluation of ^{18}F-GE-179 has demonstrated several properties that are desirable in PET radioligands, such as

FIGURE 6. V_T of ^{18}F-GE-179 for representative participant (1), as calculated by RS-ESA. Image has been smoothed by isotropic gaussian filter of 6 mm at full width at half maximum.

TABLE 4
^{18}F-GE-179 V_T as Calculated by Voxelwise RS-ESA

Region	V_T		Between-subject CV in V_T (%)
	Median	IQR	
(Whole-brain) gray matter	8.4	7.7–9.9	12.3
Putamina	10.9	9.5–12.5	14.8
Thalami	11.1	9.4–11.6	13.6
Superior frontal gyri	8.2	7.8–9.3	11.6
Occipital lobes	8.2	8.2–8.8	12.6
Cerebellum	8.3	7.4–9.5	13.7
Parahippocampal gyri	7.8	7.2–8.1	13.2

high brain uptake and acceptable between-subject variability. Quantification of V_T appears feasible within ROIs and at the voxel level. The specificity of ^{18}F-GE-179 binding requires further characterization and could potentially limit its application. Further in vivo evaluation of ^{18}F-GE-179 is warranted.

REFERENCES

1. Furukawa H, Singh SK, Mancusso R, Gouaux E. Subunit arrangement and function in NMDA receptors. *Nature.* 2005;438:185–192.
2. Sattler R, Xiang ZG, Lu WY, Hafner M, MacDonald JF, Tymianski M. Specific coupling of NMDA receptor activation to nitric oxide neurotoxicity by PSD-95 protein. *Science.* 1999;284:1845–1848.
3. Leker RR, Shohami E, Leker RR, Shohami E. Cerebral ischemia and trauma-different etiologies yet similar mechanisms: neuroprotective opportunities. *Brain Res Brain Res Rev.* 2002;39:55–73.
4. Kalia LV, Kalia SK, Salter MW, Kalia LV, Kalia SK, Salter MW. NMDA receptors in clinical neurology: excitatory times ahead. *Lancet Neurol.* 2008;7: 742–755.
5. Lau CG, Zukin RS. NMDA receptor trafficking in synaptic plasticity and neuropsychiatric disorders. *Nat Rev Neurosci.* 2007;8:413–426.
6. Sobrio F, Gilbert G, Perrio C, Barre L, Debruyne D. PET and SPECT imaging of the NMDA receptor system: an overview of radiotracer development. *Mini Rev Med Chem.* 2010;10:870–886.
7. Waterhouse RN. Imaging the PCP site of the NMDA ion channel. *Nucl Med Biol.* 2003;30:869–878.
8. Asselin MC, Hammers A, Turton D, Osman S, Koepp M, Brooks D. Initial kinetic analyses of the in vivo binding of the putative NMDA receptor ligand [C-11]CNS 5161 in humans. *Neuroimage.* 2004;22(suppl 2):T137–T138.
9. Hammers A, Asselin MC, Brooks DJ, et al. Correlation of memory function with binding of [C-11]CNS 5161, a novel putative NMDA ion channel PET ligand. *Neuroimage.* 2004;22(suppl 2):T54–T55.
10. Ahmed I, Bose SK, Pavese N, et al. Glutamate NMDA receptor dysregulation in Parkinson's disease with dyskinesias. *Brain.* 2011;34:979–986.
11. Robins EG, Zhao Y, Khan I, Wilson A, Luthra SK, Årstad E. Synthesis and in vitro evaluation of ^{18}F-labelled S-fluoroalkyl diarylguanidines: novel high-affinity NMDA receptor antagonists for imaging with PET. *Bioorg Med Chem Lett.* 2010;20:1749–1751.
12. Hu LY, Guo J, Magar SS, Fischer JB, Burke-Howie KJ, Durant GJ. Synthesis and pharmacological evaluation of N-(2,5-disubstituted phenyl)-N′-(3-substituted phenyl)-N′-methylguanidines as N-methyl-D-aspartate receptor ion-channel blockers. *J Med Chem.* 1997;40:4281–4289.
13. Biegon A, Gibbs A, Alvarado M, et al. In vitro and in vivo characterization of [3H]CNS-5161–a use-dependent ligand for the N-methyl-D-aspartate receptor in rat brain. *Synapse.* 2007;61:577–586.
14. Defrise M, Kinahan PE, Townsend DW, Michel C, Sibomana M, Newport DF. Exact and approximate rebinning algorithms for 3-D PET data. *IEEE Trans Med Imaging.* 1997;16:145–158.
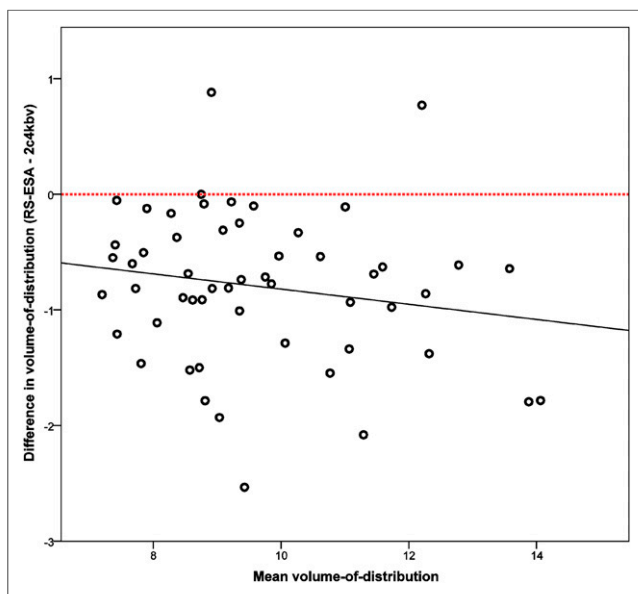
FIGURE 7. Tukey mean-difference plot for comparison of ^{18}F-GE-179 V_T as calculated by voxelwise RS-ESA and by regional 2c4kbv model. Data from 6 bilateral ROIs are shown for each participant.

15. Hammers A, Asselin MC, Turkheimer FE, et al. Balancing bias, reliability, noise properties and the need for parametric maps in quantitative ligand PET: [^{11}C]diprenorphine test-retest data. *Neuroimage.* 2007;38:82–94.

16. Turkheimer FE, Brett M, Visvikis D, Cunningham V. Multiresolution analysis of emission tomography images in the wavelet domain. *J Cereb Blood Flow Metab.* 1999;19:1189–1208.

17. Seventh annual meeting of the Organization for Human Brain Mapping: June 10–14, 2001, Brighton, United Kingdom. *NeuroImage.* 2001;13(6, suppl):1–1341.

18. Ashburner J, Friston KJ. Unified segmentation. *Neuroimage.* 2005;26:839–851.

19. Hammers A, Allom R, Koepp MJ, et al. Three-dimensional maximum probability atlas of the human brain, with particular reference to the temporal lobe. *Hum Brain Mapp.* 2003;19:224–247.

20. Heckemann RA, Keihaninejad S, Aljabar P, et al. Automatic morphometry in Alzheimer's disease and mild cognitive impairment. *Neuroimage.* 2011;56: 2024–2037.

21. Paoletti P, Neyton J, Paoletti P, Neyton J. NMDA receptor subunits: function and pharmacology. *Curr Opin Pharmacol.* 2007;7:39–47.

22. Turkheimer FE, Hinz R, Gunn RN, Aston JA, Gunn SR, Cunningham VJ. Rank-shaping regularization of exponential spectral analysis for application to functional parametric mapping. *Phys Med Biol.* 2003;48:3819–3841.

23. Cunningham VJ, Jones T. Spectral analysis of dynamic PET studies. *J Cereb Blood Flow Metab.* 1993;13:15–23.

24. Ametamey SM, Bruehlmeier M, Kneifel S, et al. PET studies of ^{18}F-memantine in healthy volunteers. *Nucl Med Biol.* 2002;29:227–231.

25. Matsumoto R, Haradahira T, Ito H, et al. Measurement of glycine binding site of N-methyl-D-asparate receptors in living human brain using 4-acetoxy derivative of L-703,717, 4-acetoxy-7-chloro-3-[3-(4-[11c] methoxybenzyl) phenyl]-2(^{1}H)-quinolone (AcL703) with positron emission tomography. *Synapse.* 2007;61:795–800.

26. Hartvig P, Valtysson J, Lindner KJ, et al. Central nervous system effects of subdissociative doses of (S)-ketamine are related to plasma and brain concentrations measured with positron emission tomography in healthy volunteers. *Clin Pharmacol Ther.* 1995;58:165–173.

27. Kumlien E, Hartvig P, Valind S, Oye I, Tedroff J, Langstrom B. NMDA-receptor activity visualized with (S)-[N-methyl-^{11}C]ketamine and positron emission tomography in patients with medial temporal lobe epilepsy. *Epilepsia.* 1999;40:30–37.

28. Owens J, Wyper DJ, Patterson J, et al. First SPET images of glutamate (NMDA) receptor activation in vivo in cerebral ischaemia. *Nucl Med Commun.* 1997;18:149–158.

29. Erlandsson K, Bressan RA, Mulligan RS, et al. Kinetic modelling of [^{123}I]CNS 1261: a potential SPET tracer for the NMDA receptor. *Nucl Med Biol.* 2003;30: 441–454.

30. Brown DR, Wyper DJ, Owens J, et al. 123Iodo-MK-801: a SPECT agent for imaging the pattern and extent of glutamate (NMDA) receptor activation in Alzheimer's disease. *J Psychiatr Res.* 1997;31:605–619.

31. Monaghan DT, Cotman CW. Distribution of N-methyl-D-aspartate-sensitive L-[^{3}H]glutamate-binding sites in rat brain. *J Neurosci.* 1985;5:2909–2919.

32. Stys PK, Lipton SA. White matter NMDA receptors: an unexpected new therapeutic target? *Trends Pharmacol Sci.* 2007;28:561–566.

33. Scherzer CR, Landwehrmeyer GB, Kerner JA, et al. Cellular distribution of NMDA glutamate receptor subunit mRNAs in the human cerebellum. *Neurobiol Dis.* 1997;4:35–46.

34. Erreger K, Dravid SM, Banke TG, Wyllie DJ, Traynelis SF. Subunit-specific gating controls rat NR1/NR2A and NR1/NR2B NMDA channel kinetics and synaptic signalling profiles. *J Physiol.* 2005;563:345–358.

35. Dravid SM, Prakash A, Traynelis SF. Activation of recombinant NR1/NR2C NMDA receptors. *J Physiol.* 2008;586:4425–4439.

36. Wyllie DJ, Behe P, Colquhoun D. Single-channel activations and concentration jumps: comparison of recombinant NR1a/NR2A and NR1a/NR2D NMDA receptors. *J Physiol.* 1998;510:1–18.

37. Rigby M, Le Bourdelles B, Heavens RP, et al. The messenger RNAs for the N-methyl-D-aspartate receptor subunits show region-specific expression of different subunit composition in the human brain. *Neuroscience.* 1996;73:429–447.

38. Forst T, Smith T, Schutte K, Marcus P, Pfutzner A, CNS Study Group. Dose escalating safety study of CNS 5161 HCl, a new neuronal glutamate receptor antagonist (NMDA) for the treatment of neuropathic pain. *Br J Clin Pharmacol.* 2007;64:75–82.

39. Buijs PC, Krabbe-Hartkamp MJ, Bakker CJ, et al. Effect of age on cerebral blood flow: measurement with ungated two-dimensional phase-contrast MR angiography in 250 adults. *Radiology.* 1998;209:667–674.

40. Foster TC. Dissecting the age-related decline on spatial learning and memory tasks in rodent models: N-methyl-D-aspartate receptors and voltage-dependent Ca2+ channels in senescent synaptic plasticity. *Prog Neurobiol.* 2012;96:283–303.